Measurement of 12C Fragmentation Cross Sections on C, O and H in the Energy Range of interest for Particle Therapy Applications

Article · February 2020

DOI: 10.1109/TRPS.2020.2972197

87 authors, including:

Ilaria Mattei
INFN - Istituto Nazionale di Fisica Nucleare

Andrey Alexandrov
INFN - Istituto Nazionale di Fisica Nucleare

Luisa Alunni Solestizi
INFN - Istituto Nazionale di Fisica Nucleare

Natasha Bartosik
University of the Arts London

This is the author's version of an article that has been published in this journal. Changes were made to this version by the publisher prior to publication.
The final version of record is available at http://dx.doi.org/10.1109/TRPMS.2020.2972197

Measurement of ^{12}C Fragmentation Cross Sections on C, O and H in the Energy Range of interest for Particle Therapy Applications.

I. Mattei[1], A. Alexandrov[6], L. Alunni Solestizi[21,7], G. Ambrosi[7], S. Argirò[8,9], N. Bartosik [8], G. Battistoni [1], N. Belcari[10,11], S. Biondi[12,13], M.G. Bisogni[10,11], G. Bruni[12], N. Camarlinghi[10,11], P. Carra[10,11], E. Catanzani [21,7], E. Ciarrocchi[10,11], P. Cerello[8], A. Clozza[14], S. Colombi[15,16], G. De Lellis[6,17,32], A. Del Guerra[10,11], M. De Simoni[5,2], A. Di Crescenzo[17,6], M. Donetti[18,8], Y. Dong[1,19], M. Durante[15], A. Embriaco[1], M. Emde[20], R. Faccini[5,2], V. Ferrero[8,9], F. Ferroni[2,5], E. Fiandrini[21,7], C. Finck[22], E. Fiorina[18,11], M. Fischetti[3,2], M. Francesconi[10,11], M. Franchini[12,13], L. Galli[11], V. Gentile[23],R. Hetzel[20], S. Hild[15], E. Iarocci[3,14], M. Ionica[7], K. Kanxheri[7], A.C. Kraan[11], V. Lante[18], A. Lauria[17,17], C. La Tessa[15,16], E. Lopez Torres[8,24], C. Massimi[12], M. Marafini[4,2], A. Mengarelli[12], R. Mirabelli[5,2,4], M.C. Montesi[17,6], M.C. Morone[25,26], M. Morrocchi[11], S. Muraro[1], L. Narici[25,26], A. Pastore[27], N. Pastrone[8], V. Patera[2,3,4], F. Pennazio[8], P. Placidi[28,7], M. Pullia[18], L. Ramello[8,29], R. Ridolfi[13,12], V. Rosso[10,11], M. Rovituso[15], C. Sanelli[14], G. Sartorelli[13,12], O. Sato[30], S. Savazzi[18], L. Scavarda[9,8], A. Schiavi[3,2], C. Schuy[31], E. Scifoni[15], A. Sciubba[3,14,4], A. Sécher[22], M. Selvi[12], L. Servoli[7], G. Silvestre[21,7], M. Sitta[29,8], R. Spighi[12], E. Spiriti[14], G. Sportelli[10,11], A. Stahl[20], S. Tomassini[14], F. Tommasino[15,16], G. Traini[5,2,4],a M. Toppi[3,14], T. Valeri[6], S.M. Valle[1], M. Vanstalle[22], M. Villa[12,13], U. Weber[31], A. Zoccoli[12,13], A. Sarti[3,2,4]

[*] corresponding author, please mail to: michela.marafini@roma1.infn.it
[1] INFN, Section of Milano - Milano, Italy
[2] INFN, Section of Roma1 - Roma, Italy
[3] Dipartimento di Scienze di Base e Applicate per l'Ingegneria (SBAI)-Roma, Italy
[4] Museo Storico della Fisica e Centro Studi e Ricerche Enrico Fermi, Roma, Italy
[5] Dipartimento di Fisica, Università di Roma "La Sapienza" - Roma, Italy
[6] INFN, Section of Napoli - Napoli, Italy
[7] INFN, Section of Perugia - Perugia, Italy
[8] INFN, Section of Torino - Torino, Italy
[9] Dipartimento di Fisica, Università di Torino - Torino, Italy
[10] Dipartimento di Fisica, Università di Pisa - Pisa, Italy
[11] INFN, Section of Pisa - Pisa, Italy
[12] INFN, Section of Bologna - Bologna, Italy
[13] Dipartimento di Fisica, Università di Bologna - Bologna, Italy
[14] INFN, Laboratori Nazionali di Frascati, Frascati, Italy
[15] INFN-TIFPA, Trento Institute for Fundamental Physics and Applications, Trento, Italy
[16] Dipartimento di Fisica, Università di Trento - Trento, Italy
[17] Dipartimento di Fisica, Università di Napoli - Napoli, Italy
[18] Centro Nazionale di Adroterapia Oncologica (CNAO), Pavia, Italy
[19] Dipartimento di Fisica, Università di Milano - Milano, Italy
[20] RWTH Aachen University, Physics Institute III B, Aachen, Germany
[21] Dipartimento di Fisica e Geologia, Università di Perugia - Perugia, Italy
[22] Université de Strasbourg, CNRS, IPHC UMR 7871, F-67000 Strasbourg, France
[23] Gran Sasso Science Institute, L'Aquila, Italy
[24] CEADEN, Havana, Cuba
[25] Dipartimento di Fisica, Università di Roma "Tor Vergata" - Roma, Italy
[26] INFN, Section of Roma Tor Vergata - Roma, Italy
[27] INFN, Section of Bari - Bari, Italy
[28] Dipartimento di Ingegneria, Università di Perugia - Perugia, Italy
[29] Dipartimento di Scienze e Innovazione Tecnologica, Università Piemonte Orientale-Alessandria, Italy
[30] Department of Physics, Nagoya University - Nagoya, Japan
[31] Gesellschaft für Schwerionenforschung (GSI) - Darmstadt, Germany
[32] CERN, Geneva, Switzerland

***Abstract*—In a carbon ion treatment the nuclear fragmentation of both target and beam projectiles impacts on the dose released on the tumour and on the surrounding healthy tissues. Carbon ion fragmentation occurring inside the patient body has to be studied in order to take into account this contribution. These data are also important for the development of the range monitoring techniques with charged particles. The production of charged fragments generated by carbon ion beams of 115-353 MeV/u kinetic energy impinging on carbon, oxygen and hydrogen targets has been measured at the CNAO particle therapy center (Pavia, Italy). The use of thin targets of graphite (C), PMMA ($C_2O_5H_8$) and polyvinyl-toluene (plastic scintillator, C_bH_a) allowed to measure fragments production cross sections, exploiting a Time of Flight (ToF) technique. Plastic scintillator detectors have been used to perform the ToF measurements, while LYSO crystals have been used for the deposited energy measurement and to perform particle identification. Cross sections have been measured at 90 and 60 degrees with respect to the beam direction. The measured proton, deuteron and triton differential production cross sections on C, O and H, obtained exploiting the target subtraction strategy, are presented here as a function of the fragment kinetic energy.**

***Index Terms*—Scintillators Radiation Detectors for medical applications Radiation Therapy Clinical/preclinical evaluation/application studies Therapy imaging Clinical/preclinical evaluation/application studies**

INTRODUCTION

PARTICLE Therapy (PT) is a well established external radiotherapy technique that exploits light charged hadron beams (as protons and carbon ions) to treat solid tumours. PT is particularly suitable in case of tumours located close to organs at risk, as well as for deep-seated or radio resistant cancers [1]. The maximum dose deposition is concentrated in

This is the author's version of an article that has been published in this journal. Changes were made to this version by the publisher prior to publication.
The final version of record is available at http://dx.doi.org/10.1109/TRPMS.2020.2972197

a very narrow region (Bragg Peak, BP) where the projectiles stop and is characterized by a high biological effectiveness in killing cancerous cells, especially in the case of ^{12}C ion treatments [2]. On the other hand, hadrons with mass number $A > 1$ undergo fragmentation when interacting with the patient body, causing a dose tail beyond the BP [3]. Currently, the algorithms that take into account the projectile fragmentation in the Treatment Planning Systems (TPS) implementation are affected by several uncertainties. Both the analytical and the Monte Carlo (MC) simulations based approaches [4]–[6] suffer from the limited precision available on the production fragmentation cross section measurements at ^{12}C ion beam therapeutic energies ($80 - 400$ MeV$/u$). Such uncertainties lead to an uncertainty in the Relative Biological Effectiveness (RBE) prediction. Recent cross section measurements have been performed by several research groups [7]–[10] but the configuration of high beam energies (> 95 MeV$/u$) and large detection angles with respect to the incoming beam direction ($> 45°$) has not been yet thoroughly explored. Cross sections for the production of charged fragments at large detection angles are of interest also for applications exploiting such particles for online beam range monitoring purposes [11]–[17]. In this paper, the cross section measurements for the production of protons (p), deuterons (d) and tritons (t) in the nuclear interactions of ^{12}C ion beams on carbon, oxygen and hydrogen nuclei are reported. The experimental configurations in terms of beam energy and target are described in section I together with the experimental setup. Section II is dedicated to the description of the data analysis strategy for the cross section measurements and in section III the results are presented. The measurements have been performed at the CNAO therapy center (Pavia, Italy) [1].

I. Experimental Setup

Fragmentation cross sections of C-C, C-O, C-H for the production of secondary fragments at large angles, *i.e.* $\theta = 60° - 90°$ with respect to the incoming beam direction, have been measured using ^{12}C ion beams impinging on C, O and H targets. The beam energy has been chosen in the energy range $[100 - 350]$ MeV$/u$ of interest for PT applications.

As pure H and O targets are not easy to handle in a clinical environment, where the safety standards come from the operation inside a treatment room like the one used at CNAO, thin targets of PMMA ($C_5O_2H_8$), plastic scintillator (C_bH_a) and pure graphite (C) were used to perform the measurements. The cross sections of interest have hence been computed using the subtraction method (see section II for details), a well known procedure in the field [7]–[9].

The data taking experimental setup is shown in Fig. 1. It consists of a thin target (see Tab. I for details) and two instrumented arms, equipped for the secondary fragments detection, that are respectively placed at 90 (Arm1) and 60 degrees (Arm2) with respect to the incoming beam direction.

The thin targets - PMMA, plastic scintillator and graphite - have been placed, alternatively, on the beam line and have been used to study the fragmentation production of carbon ion beams of therapeutic intensity ($\sim 10^8$ ions/s). The composition, thickness and density of each target is shown in Table I. For the plastic scintillator (EJ-212) the numbers of H and C atoms (a and b) are respectively $5.17 \cdot 10^{22}$ H cm^3 and $4.69 \cdot 10^{22}$ C cm^3.

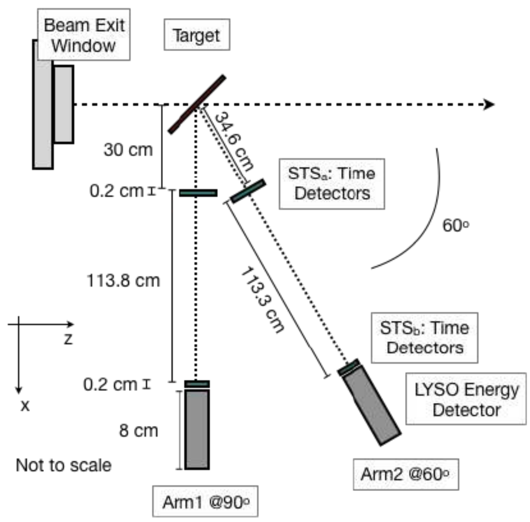

Figure 1. Sketch of the experimental setup (not to scale). The employed detectors are shown, as well as their dimensions and relative distances.

Both arms (Arm1 and Arm2) were instrumented with two thin plastic scintillator detectors (STS$_a$ and STS$_b$) used for the fragments Time of Flight measurement. Each *Time Detector* was followed by a LYSO crystal to perform energy deposit measurements. The relative distances between the different detectors are reported in Fig. 1.

Target	Composition	Thickness $[mm]$	th_Y $[mm]$	Density $[g/cm^3]$
PMMA	$C_5O_2H_8$	2	2.8	1.19
Graphite	C	1	1.4	0.94
Pla.Scint.	C_bH_a	2	2.8	1.024

Table I
COMPOSITION AND SPECIFIC TARGET PARAMETERS. THE THICKNESS AND DENSITY OF THE TARGETS HAVE BEEN MEASURED BEFORE AND AFTER THE DATA TAKING.

Targets were positioned at $45°$ with respect to the beam direction and hence the effective thickness (th_Y in the table and in the following) seen by the beam was the target thickness multiplied by a factor $\sqrt{2}$. The graphite target, prepared by the *target workshop* of the INFN LNS [2], was characterized by a low density. The thicknesses and densities of the targets have been measured and cross-checked against the material datasheets.

The target longitudinal dimensions have been chosen to be as thin as possible in order to reduce the absorption of the produced fragments by the target itself. The fragments energy loss when crossing the target has been taken into account in the analysis exploiting a dedicated MC simulation performed with the FLUKA [18], [19] software (details are

[1]Fondazione CNAO - Centro Nazionale di Adroterapia Oncologica

[2]Laboratori Nazionali del Sud - Catania, Italy

given hereafter).

Each target has been impinged by about $5 \cdot 10^9$ carbon ions for each energy dataset and the signals from the two arms have been acquired simultaneously. Five carbon ion beam energies have been studied: $115.23, 152.71, 221.45, 280.97, 352.86$ MeV/u. The average energy loss by the carbon ions in the targets is $\sim 3, 2, 1, 0.7$ and 0.5% respectively for the different datasets. The beam energies in the following tables are indicated in a more compact way as $115, 153, 221, 281, 353$ MeV/u.

The timing detectors, STS_a^1, STS_b^1 and STS_a^2, STS_b^2 (Fig. 1), are thin plastic scintillator slabs (BC412 S.Gobain). Their dimensions are respectively: $4.0 \times 4.0 \times 0.2$ cm^3 for $\mathrm{STS}_a^{1,2}$, $8.0 \times 4.0 \times 0.2$ cm^3 for STS_b^1 and $17.0 \times 4.0 \times 0.2$ cm^3 for STS_b^2. The signals readout were performed by means of a PMT H10580 (Hamamatsu).

The $\mathrm{LYSO}_{1,2}$ crystals ($4.0 \times 4.0 \times 8$ cm^3) (Scionix Holland V40B80) were used to perform the deposited energy measurements.

The data acquisition system (DAQ) has been implemented using NIM and VME modules. The energy deposit in the scintillators has been measured by means of two 12-bit ADC V792N: one acquired the plastic scintillator detectors signals and was configured setting a 150 ns gate (short gate) and one acquired the LYSO detectors signals and was configured with a 800 ns gate (long gate). To increase the dynamic range of the long gate ADC, two consecutive attenuation stages (allowing an amplitude reduction of a factor $1/2$ and $1/12$ respectively), have been applied to the signals. The discriminated signals from the timing detectors were measured using a multi-hit TDC (V1290, resolution of 25 ps). Low threshold discriminators were used and the discriminated signal had a length of 150 ns preventing the multiple counting of afterpulses that were observed in a 100 ns time window. A V560 scaler was exploited for rate counting measurements. The VME modules system is interfaced with the DAQ pc using a VME Bridge V2718 module and a fibre optical connection. The DAQ system trigger was implemented as the OR of the two Arms trigger signals, while the single Arm trigger was built as the logic AND between STS_a and STS_b discriminated signals, i.e. the time coincidence of STS_a and STS_b in a time window of 150 ns.

The Arm1 (Arm2) trigger rate ranged between $\sim$ 30 (200) Hz and $\sim$ 90 (600) Hz, and increased with the beam energy. The occurrence of multi-trigger events (events in which more than one trigger signal is registered in a time window of 2 µs) has been evaluated exploiting the multi-hit TDC: for both arms their occurrence was measured to be less than 2‰, for all the datasets.

II. Measurements strategy

The differential cross section $d\sigma(^A_ZX)/dE_k$ as a function of the fragment kinetic energy at production dE_k measured at $\theta = 60°, 90°$ is defined as:

$$\frac{1}{\Delta\Omega}\frac{d\sigma}{dE_k}(^A_ZX) = \frac{1}{4\pi} \cdot \frac{1}{N_Y\ \Delta E_k} \cdot \frac{N_{^A_ZX}(E_k)}{N_{^{12}C}} \cdot \frac{1}{\epsilon} \quad (1)$$

where the number of specific fragments, $N_{^A_ZX}(E_k)$, is normalised to the number of incoming carbon ions, $N_{^{12}C}$, 4π is the solid angle in steradiant and ΔE_k is the fragment kinetic energy bin size. The number of scattering centres, N_Y, in a Y target is defined as:

$$N_Y = \frac{\rho_Y \cdot th_Y \cdot N_A}{A_Y} \quad (2)$$

where A_Y is the atomic mass number, N_A the Avogadro number, ρ_Y the target density and th_Y is the thickness of the crossed target (see Table. I). N.B.: the $1/\Delta\Omega$ factor has been hidden from the following $d\sigma/dE_k$ formulas to ease the text readability.

The fragments production cross section, $\sigma(^A_ZX)$, is therefore obtained integrating $d\sigma(^A_ZX)/dE_k$ in a specific energy range.

The detection and analysis selection efficiency (ϵ) is explicitly shown in Eq.(1). This efficiency is defined as:

$$\epsilon = \epsilon_{Det} \cdot \epsilon_{Sel} \cdot \epsilon_{DT} \quad (3)$$

where ϵ_{Det} takes into account the geometrical acceptance as well as the trigger and detection efficiencies (see section II-C1), ϵ_{Sel} is accounting for the efficiency in identifying the fragments (see section II-C2) and ϵ_{DT} takes into account the DAQ system dead time. The DAQ dead time was measured to be in the $2-8\%$ range depending on the beam rate, and has been assumed to be constant in the data analysis for each data acquisition/fixed energy data sample.

The number of delivered primary carbon ions ($N_{^{12}C}$) has been recorded for each dataset by the CNAO dose delivery system (Table II). The number of ions is evaluated from the measurement of the charge released by the beam in the ionisation chambers and is affected by an uncertainty that is related to the current measurement precision and to the dose-current conversion systematic uncertainty. The relative uncertainty on $N_{^{12}C}$ (4%) is hence the convolution of the uncertainty on the stopping power determination [20] and on the dose measurements [21]. A possible additional contribution to the systematic uncertainty, coming from the monitoring system measurement stability [22], was found to be negligible (0.2%).

$N_{^{12}C}$	$\cdot 10^6$	$\cdot 10^6$	$\cdot 10^6$	$\cdot 10^6$	$\cdot 10^6$
Target	115 [MeV/u]	153 [MeV/u]	221 [MeV/u]	281 [MeV/u]	353 [MeV/u]
PMMA	49866	46512	49395	49601	42000
Graphyte	49454	46583	47484	47288	49328
Pla. Scint.	49728	50600	49347	49787	49653

Table II
Number of carbon ions impinging on the target for the different datasets.

The proton, deuteron and triton production differential cross sections evaluated using C, O and H elemental targets are obtained combining the ones measured using the three different thin targets: PMMA, graphite and plastic scintillator (PS). The graphite target gives direct access to the C-C fragmentation cross section (Eq. 4), the C on H fragmentation cross section is evaluated combining the graphite and PS measurements (Eq. 5) while the C on O fragmentation cross section is evaluated exploiting the PMMA target (Eq. 6). The relations between the elemental cross sections and the ones measured using thin targets are detailed hereafter:

$$\frac{d\sigma_C}{dE_k} = \frac{d\sigma^{Graphite}}{dE_k} \tag{4}$$

$$\frac{d\sigma_H}{dE_k} = \frac{1}{0.524} \cdot [\frac{d\sigma^{PS}}{dE_k} - 0.476 \cdot \frac{d\sigma_C}{dE_k}] \tag{5}$$

$$\frac{d\sigma_O}{dE_k} = \frac{1}{2} \cdot [\frac{d\sigma^{PMMA}}{dE_k} - 8 \cdot \frac{d\sigma_H}{dE_k} - 5 \cdot \frac{d\sigma_C}{dE_k}] \tag{6}$$

The numerical factors used in Eq. 5 (0.524 and 0.476) have been extracted from the data-sheet material composition and are reported in Table I.

The p,d and t production cross section measurements as a function of the production kinetic energy require an accurate fragment identification algorithm. The energy measurements and the identification algorithms are detailed in the following paragraphs (§ II-B and § II-A).

A. *Fragment Identification*

In order to separate the different fragments populations, three observables can be exploited:

1) E: the energy deposited in the LYSO crystal;
2) ΔE: the energy loss in the STS$_{a,b}$;
3) ToF: the Time of Flight between the STS$_a$ and STS$_b$ scintillators.

The measurements of E and ΔE are performed integrating the detect signals and are shown in terms of the resulting charge (pC) as measured by the ADC modules (see section I). The experimental setup has been carefully included in a Monte Carlo (MC) simulation, performed using the FLUKA software, of the measurements described in this manuscript . The measured energy and ToF resolution have been included in the simulation. The simulation has been used to study the impact of the fragment identification algorithms on the final measurement and, as detailed in section II-C, for the efficiency evaluation.

The deposited energy in the LYSO crystals, as a function of the ToF, is shown in Fig. 2 where data and MC are superimposed. The dashed lines are showing the central values of the narrow bands related to the different fragments populations identified using the truth matching information in the MC simulation. The red dots, instead, are obtained performing the full analysis chain on the MC events taking into account also the detectors resolution, both in time and energy. The bands related to the protons show a discontinuity at very high energies and ToF smaller than ~ 8 ns as in this case the fragments are not fully contained in the LYSO crystal and hence the related energy deposit is only partial. The deposited energy in the analysis presented hereafter is only used for fragment identification purposes. The kinetic energy of each fragment, instead, is obtained directly from the ToF measurement (see Sect. II-B). The MC simulation was used to tune the fragment identification algorithms and assign the relative systematic uncertainty, as explained in detail below (§ II-C2).

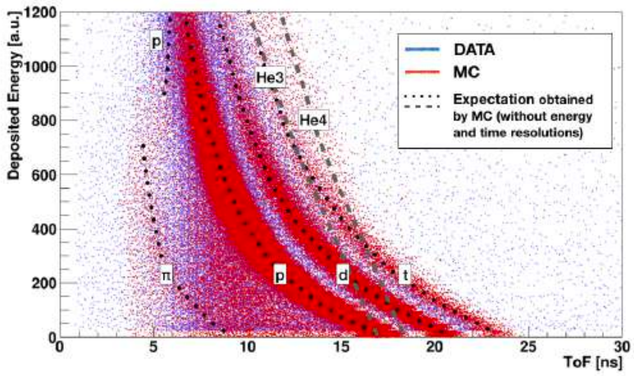

Figure 2. The deposited energy in the LYSO crystal is shown as a function of the measured particles time of flight for data (blue) and MC (red). The MC populations central values are shown by the dotted lines. The deposited energy is shown in arbitrary units.

The combined use of the E, ΔE (in terms of deposited charge - QDC) and ToF variables allowed for a clean and efficient fragment population separation in the data. Fragments are firstly separated as a function of their charge (Z), and hence the different contribution to each population (e.g. p, d, t and pions on one side and He3, He4 on the other one) are identified.

This separation can be effectively achieved by exploiting the ΔE in the STS$_{a,b}$ distributions as a function of the fragments ToF and E (for redundancy). An example is shown in Fig. 3 (top) for the 60 degrees configuration. The red lines are showing the selection bands identified in the plane. The p, d, t identification is performed exploiting the E vs $1/ToF$ distribution, as shown in Fig. 3 (bottom). Protons and deuterons are reasonably abundant in all the datasets (they respectively contribute to the 80% and 15% of the total number of detected fragments at $60°$) while, as expected, at large angles the triton contribution is much smaller (5% of the fragments at $60°$). Pions appear only in the two most energetic carbon ion beam configurations at 281 and 353 MeV/u consistently with the known π production threshold (~ 290 MeV/u) in nucleus-nucleus interactions. Since the number of acquired pions and fragments with charge greater than one is very low ($Z = 2$ occurs in less than 2% of the cases, at $60°$), in the following we report the differential cross section only for p, d and t.

The particle identification (PID) selection, shown in Fig. 3, has been applied to the events acquired by both arms also exploiting also the STS$_a$ information (that is qualitatively consistent with what shown for the STS$_b$). The separation curves have been optimised exploiting the full statistics acquired for the two arms. The PID result for the Arm2 sample in the E vs ToF plane is shown in Fig. 4, where the selected p, d, and t fragments populations are represented by the blue, green and purple dots superimposed to the full data distribution after the removal of $Z > 1$ fragments. The PID method efficiency evaluation is detailed in section II-C2. A systematic uncertainty related to the PID method has been computed

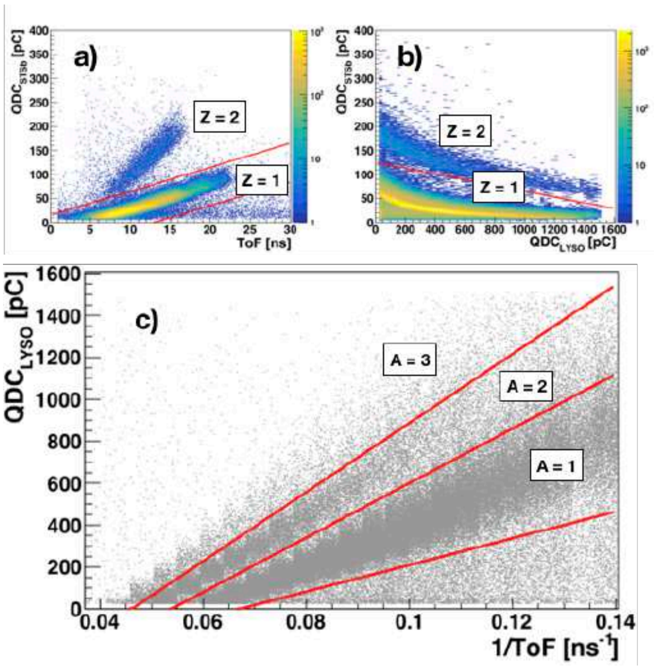

Figure 3. a) Top Left. The energy loss in the STS_b (in pC) is shown as a function of the ToF for the measured particles. b) Top Right. The energy loss in the STS_b (in pC) is shown as a function of E (in pC). c) Bottom. The $Z = 1$ fragments selected from a) and b) are separated in mass ($A = 1$, $A = 2$ and $A = 3$) using the bands identified by the red lines. Data refer to the 60 degrees sample.

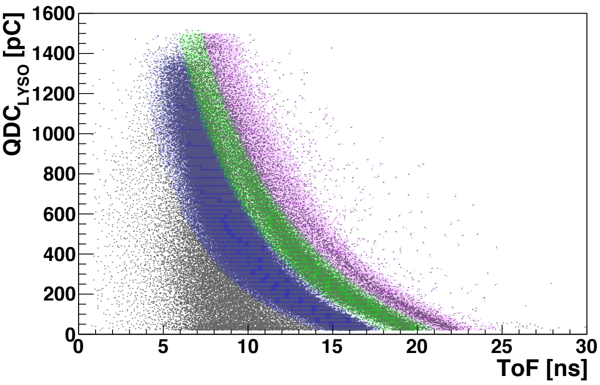

Figure 4. E (in pC) is shown as a function of the measured particles ToF for the 60 degrees sample (grey dots). The populations of p (blue dots), d (green dots) and t (purple dots) fragments are identified exploiting the E and $1/ToF$ measurements after having removed the contribution from fragments with $Z > 1$ (see the text for details).

defining 'hard' and 'soft' selections by varying the slope of the separation curves by 1% (for a detailed discussion see section III-B).

B. Kinetic Energy Measurement

Once the fragments have been identified it is possible to compute their kinetic energy (E_{kin}^{meas}) exploiting the following relations:

$$E_{kin}^{meas} = m_i \cdot (\gamma_i - 1);$$

where

$$\gamma_i = (1. - \beta_i^2)^{-1/2} \quad , \quad \beta_i = L/(ToF_i \cdot c)$$

and m_i are the masses of the fragments $i = p, d, t$, L is the distance between the two STS, c is the speed of light and ToF is the measured time of flight.

As the kinetic energy evaluation is performed using the ToF, its resolution is hence function of both the ToF resolution and depends on the fragments mass. The ToF resolution has been measured be means of a dedicated run where the STS detectors were placed at a distance of 20 ± 5 mm. The STS_a and STS_b time difference distribution is a Gaussian centred in zero (the different cables length and electronic response was taken into account), and the measured sigma has been used as an evaluation of the ToF resolution: 590 ps and 430 ps for Arm1 and Arm2 respectively. The kinetic energy resolution as a function of the fragments kinetic energy ranges from 2% up to 13% for the 90 degrees and 60 degrees experimental setup, depending on the fragment species (see Appendix A). The resolution worsens with increasing energy, as expected, for protons, deuterons and tritons.

The kinetic energy spectra are shown using variable size bins that have been chosen as a compromise between the energy resolution and the available statistics in each bin. Since the time resolution and the statistics of the two different arms is different, the bin size has been chosen differently for the two angular setups.
In order to give the cross section results as a function of the kinetic energy at production, the E_{kin}^{meas} from ToF has been corrected for the energy loss in the target and in the STS_a exploiting the FLUKA MC simulation developed for the detection efficiency evaluation (see section II-C1). Fig.5 shows an example of the ToF distribution (top) and of the related kinetic energy E_{kin} distribution at production (bottom) for Arm2, graphite target, 353 MeV/u carbon ion beam. The protons are shown in blue, deuterons in green and tritons in purple.

C. Efficiency Evaluation

The efficiency ϵ_{Det} and ϵ_{Sel} (see eq. 3) have been evaluated using two dedicated Monte Carlo simulations developed using the FLUKA software [18], [19].

1) Detection Efficiency: ϵ_{Det} is defined as the product of the detection, trigger and geometrical efficiencies. While the improvement, and fine tuning, of the fragments production models implemented inside the MC software tools is the scope of the reported cross section measurements, their impact in the calculation of the detection efficiency is negligible. The ϵ_{Det} result relies only on the simulation of the p, d and t transportation inside matter and not on their production models.

An isotropic source has been used to simulate the production of p, d and t fragments inside the different targets (PMMA, graphite, plastic scintillator). Fragments were produced with a

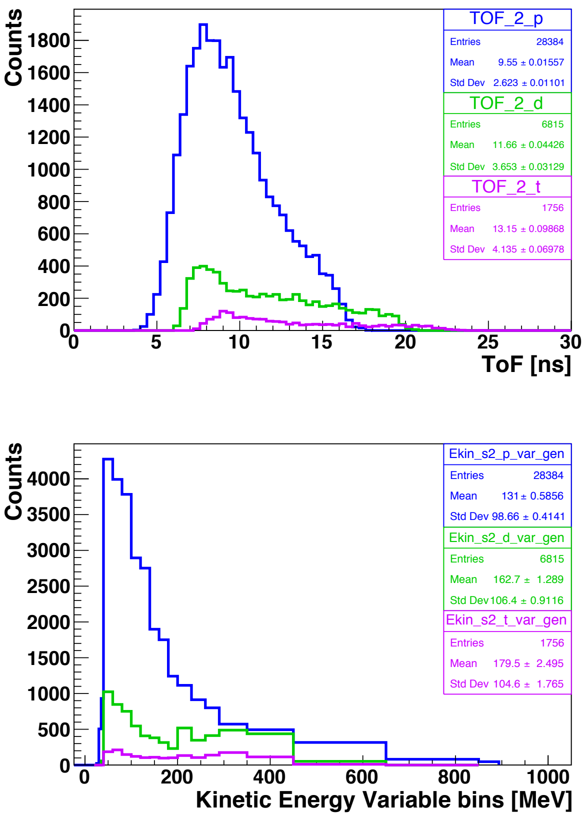

Figure 5. Top: the protons (blue line), deuterons (green line) and tritons (purple line) ToF distributions. Bottom: kinetic energy distributions at production, obtained from the ToF ones as explained in the text. Data refers to Arm2, graphite target and C-ion beam of 353 MeV/u energy.

uniform kinetic energy spectrum between 5 MeV (10 MeV, 15 MeV) and 1 GeV (2 GeV, 3 GeV). The spatial distribution of the source was obtained from the full simulation of the interaction of ^{12}C ions of different energies with the three different targets used in the experimental setups and is, for all cases, a Gaussian with a $\sigma_{x,y,z} \sim 2$ mm.

Each detector of the experimental setup (for both arms) has been included in the simulation. The experimental energy threshold for each detector ($E^{thr}_{STS_a} = E^{thr}_{STS_b} = 5$ MeV, $E^{thr}_{LYSO} = 24$ MeV) has been considered as well as the experimental timing coincidence window (150 ns) between the STS detectors to perform the trigger of the simulated events as in the experimental data. The final detection efficiency ϵ_{Det} is computed as a function of the fragment type ($u = p, d, t$) and of its production kinetic energy E_{kin} (see section II-B) and it is defined as:

$$\epsilon^u_{Det}(E_{kin})_i = \left(\frac{N^u_{meas}}{N^u_{gen}}\right)_i \tag{7}$$

where N^u_{meas} is the number of fragments of type u in the *i-th* E_{kin} bin, traversing all the arm detectors (STS$_a$, STS$_b$ and LYSO), with a deposited energy in each detectors that is larger than the corresponding thresholds and satisfy the trigger selection algorithm requirements that implement the experimental data-like acquisition conditions. N^u_{gen}, needed for the efficiency calculation, is instead the number of fragments of type u generated in the *i-th* E_{kin} bin.

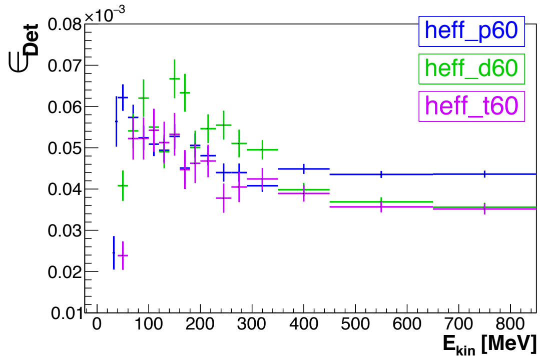

Figure 6. The ϵ_{Det} efficiencies as a function of the fragment kinetic energy E_{kin} at production for p (blue), d (green) and t (purple) fragments are shown for Arm2 (60°), PMMA target. The E_{kin} bin widths are defined in the very same way as the ones used for experimental data analysis (see section II-B).

In Fig. 6 the ϵ_{Det} efficiency as a function of the fragment kinetic energy E_{kin} is shown for p (blue), d (green) and t (purple) fragments generated in a PMMA target and for the 60° detection arm.

2) Selection Efficiency: The selection efficiency ϵ_{Sel} was computed from a full MC simulation of the different experimental setups by measuring the probability that a fragment of type i is measured in the region j ($i, j = p, d, t$ for protons, deuterons and tritons respectively) of the $(E - 1/ToF)$ plane. The diagonal values of the mixing matrix $\epsilon^{ij}_{mix} = N_{ij}/N_i$, where N_{ij} is the number of fragments i mis-identified as fragments j in the region j normalised to the total number of fragments N_i generated in the $(E - 1/ToF)$ plane, have been used to evaluate ϵ_{Sel}. The mixing matrix is defined as follows:

$$\epsilon_{mix} = \begin{pmatrix} \epsilon^{pp} & \epsilon^{pd} & \epsilon^{pt} \\ \epsilon^{dp} & \epsilon^{dd} & \epsilon^{dt} \\ \epsilon^{tp} & \epsilon^{td} & \epsilon^{tt} \end{pmatrix} \tag{8}$$

The definition of the i and j regions is detailed in section II-A. The off-diagonal matrix elements that are significantly different from zero are used in order to correct the estimate of $N_{^A_ZX}$ (see Eq. 1) for the wrong fragment identification assignment (cross feed between fragments population).

The mixing matrix has been computed for the two detection angle configurations. As expected, the results, listed in Tab. III, show a low dependency on the beam kinetic energy. The ϵ^{pt} element is consistent with zero and therefore is not shown in the Table.

While the diagonal elements impact directly the differential cross section measurements (presented in section III-A), the off-diagonal elements have been used to evaluate systematic corrections presented in section III-B.

III. Results and Discussion

In Fig. 7 the p production cross section in PMMA (top panel), graphite (middle panel) and plastic scintillator (bottom

Table III
PARTICLE IDENTIFICATION EFFICIENCY: SELECTION EFFICIENCIES EVALUATED FOR BOTH 90° AND 60° DETECTION CONFIGURATIONS.

E^{C}_{kin} $[MeV/u]$	ϵ^{pp} [%]	ϵ^{dd} [%]	ϵ^{tt} [%]
90^o			
115	95 ± 5	89 ± 9	85 ± 12
153	95 ± 5	85 ± 14	91 ± 6
221	94 ± 5	85 ± 12	86 ± 10
281	94 ± 5	84 ± 12	71 ± 31
353	94 ± 5	84 ± 14	81 ± 15
60^o			
115	95 ± 4	78 ± 21	76 ± 32
153	95 ± 5	77 ± 22	83 ± 17
221	95 ± 5	75 ± 23	73 ± 32
281	95 ± 5	75 ± 24	76 ± 26
353	94 ± 5	75 ± 24	69 ± 37

Table IV
PARTICLE IDENTIFICATION EFFICIENCY: OFF DIAGONAL ELEMENTS EVALUATED FOR BOTH THE 90° AND 60° DETECTION CONFIGURATIONS.

E^{C}_{kin} $[MeV/u]$	ϵ^{dp} [%]	ϵ^{tp} [%]	ϵ^{pd} [%]	ϵ^{td} [%]	ϵ^{dt} [%]
90^o					
115	6 ± 7	-	2 ± 2	12 ± 13	5 ± 7
153	10 ± 15	2 ± 3	1 ± 2	5 ± 4	4 ± 5
221	4 ± 4	3 ± 4	2 ± 3	11 ± 10	7 ± 6
281	5 ± 3	2 ± 2	2 ± 3	8 ± 6	8 ± 7
353	4 ± 2	1 ± 1	2 ± 2	10 ± 10	7 ± 7
60^o					
115	4 ± 3	2 ± 2	1 ± 2	3 ± 4	13 ± 13
153	4 ± 2	2 ± 2	1 ± 2	2 ± 2	16 ± 16
221	4 ± 4	2 ± 2	1 ± 2	8 ± 14	17 ± 17
281	4 ± 3	3 ± 3	1 ± 2	10 ± 19	16 ± 16
353	4 ± 3	5 ± 6	2 ± 3	10 ± 14	17 ± 17

panel) thin targets, computed from eq. 1, are shown as a function of the proton kinetic energy at production. Fragment yields take into account the selection, detection and geometrical efficiencies and are corrected for the acquisition dead time. No correction for the cross feed between different particle identification hypotheses (the off-diagonal ϵ_{mix} matrix) is implemented at this level. The y-axis error bars reflect only the statistical uncertainty. The spectra are shown with bins of variable size: the x-axis bin sizes were defined accounting for the kinetic energy resolution and population of each bin (see section II-B). The spectra obtained for the beam energies under study are superimposed (nuance of colors). It can be noticed that, as expected, the spectra end point increases with the beam energy. Measurements with both graphite and plastic scintillator targets show, as expected, yields that are about one order of magnitude smaller when compared with the PMMA one. Similar spectra are obtained for the 90 degrees configuration but the collected statistics in this case in one order of magnitude lower with respect to the data collected at 60 degrees.
The same analysis has been performed for d and t fragments and the elemental cross sections have been retrieved from the cross section of C and of composite targets for all the fragment types. Final results are presented in the following sections.

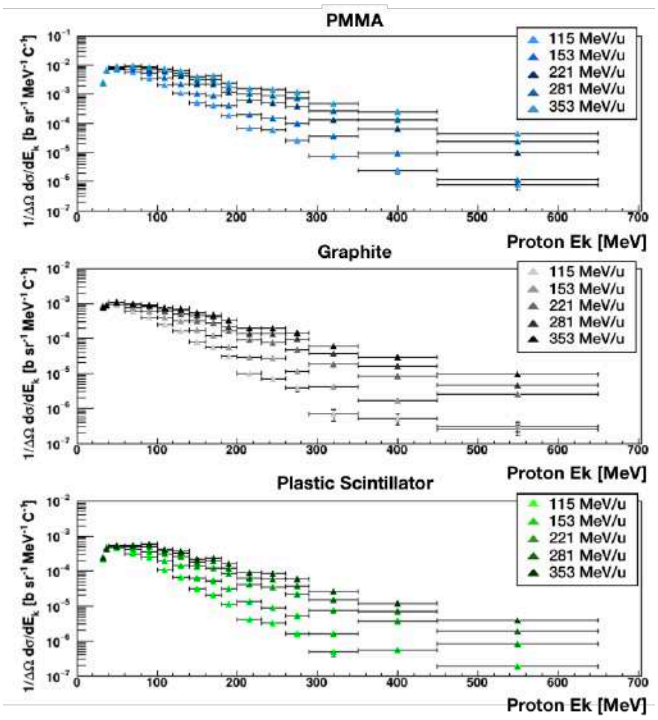

Figure 7. The differential cross sections for p production in PMMA (top), graphite (middle) and plastic scintillator (bottom) thin targets are shown for different carbon ion beam energies (nuance of colour). The data refer to the 60 degrees configuration.

A. Differential Cross Sections as a Function of the Fragment Kinetic Energy

The p, d and t production differential cross section as a function of their production kinetic energy have been obtained for each element (C, O and H) combining the information of the different targets, according to equation 4, 5, 6.

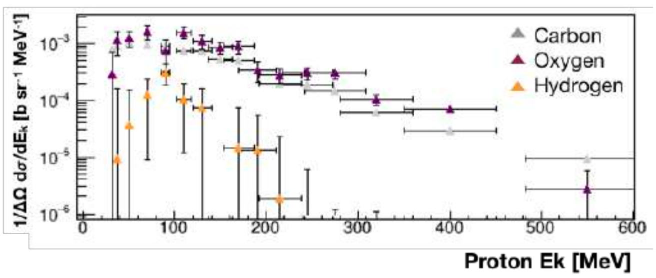

Figure 8. The differential cross section for protons production in carbon (gray), oxygen (magenta) and hydrogen (orange) as a function of the fragment kinetic energy are reported. The data refer to the 60 degrees configuration and are relative to a carbon ion beam of 353 MeV/u energy.

Fig. 8 shows, as an example, the p production differential cross section evaluated at 60 degrees when carbon ions of 353 MeV/u kinetic energy are impinging on carbon (gray), oxygen (magenta) and hydrogen (orange) elements. The low statistics available when performing the H cross section evaluations determines the large error bars seen in the figure. The differential cross sections as a function of the production kinetic energy are reported for each target element, setup and beam energy in appendix A for p, d and t. The horizontal error bars of Fig. 8 are representative, consistently with what shown in the appendix tables (A), of the energy resolution computed assuming a kinetic energy equal to the bin centre one (and this is needed to account the resolution dependence on the production kinetic energy).

B. Cross Sections as a Function of the Beam Energy

The fragments integrated cross sections in the kinetic energy range $[25-600]$ MeV have been calculated for p, d and t both at 90 and 60 degrees. The obtained results account for the off-diagonal mixing matrix efficiency, described in Sec. II-C2, that evaluates the probability of mis-identifying a fragment i as a fragment j (when $i \neq j$ with $i, j = p, d, t$) when applying the PID selection algorithms. The statistical uncertainty on the ϵ^{ij}_{mix} values was propagated as a systematic uncertainty on the integrated cross section, since ϵ_{mix} was computed from a FLUKA MC simulation with a limited statistics. The contribution to the total uncertainty ranges from $4-5\%$ in the case of protons up to several thousand of percent in the case of tritons. Other systematic uncertainty sources that were considered in the analysis are the evaluation of the number of carbon ions (see section I) and the PID selection functions. The slope on the PID selection function was been varied by $\pm 1\%$ in order to obtain "hard" and "soft" selection bands. The analysis was redone and the p, d and t populations were re-evaluated to assign a final systematic uncertainty by measuring the results variations. The relative uncertainty on the total cross sections from this systematic source ranges from 0.5% for protons at $90°$ up to 10% for tritons at $60°$. In Tables V, VI and VII the measured cross section for p, d and t are reported. The uncertainty reported in the Tables is the squared sum of the statistical and systematic contributions. Fig. 9 and 10 show the p, d and t fragments integrated production cross section as a function of the beam energy at 90 and 60 degrees, respectively.

The carbon (gray) and oxygen (magenta) cross sections are, as expected, one and two orders of magnitude higher than the hydrogen (orange) ones, depending on the arm and on the fragment species.

As expected, at $60°$, p, d and t are one order of magnitude more abundant with respect to the $90°$ configuration.

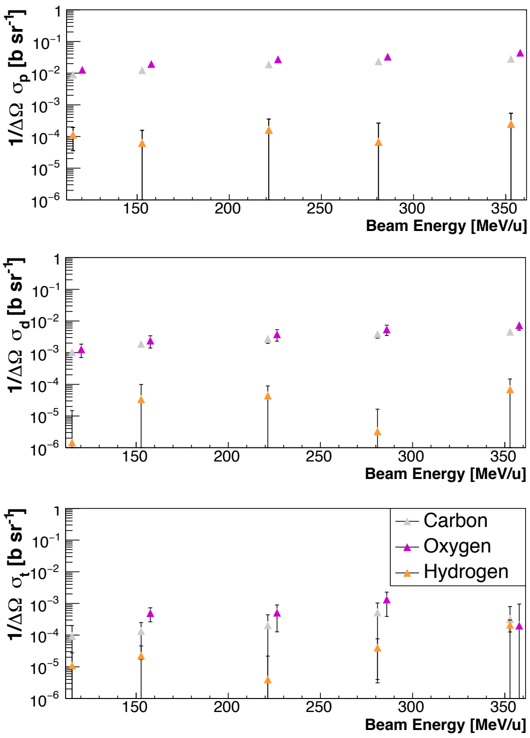

Figure 9. The cross sections integrated in the $[20-600]$ MeV fragment kinetic energy range for p (top), d (middle) and t (bottom) fragments produced in carbon (gray), oxygen (magenta) and hydrogen (orange) elements are shown as a function of the beam kinetic energy. The data refer to the 90 degrees arm. A 5 MeV shift has been applied for oxygen data in order to ease the readability of the results.

Table V
INTEGRATED PROTON PRODUCTION CROSS SECTIONS IN THE $[20-600$ MeV$]$ FRAGMENT KINETIC ENERGY RANGE MEASURED AT DIFFERENT BEAM ENERGIES AND AT DIFFERENT ANGLES.

E^{C}_{kin} $[MeV/u]$	σ^{p}_{C} [barn $/sr$]	σ^{p}_{O} [barn $/sr$]	σ^{p}_{H} [barn $/sr$]
90^o	$\cdot 10^{-3}$	$\cdot 10^{-3}$	$\cdot 10^{-5}$
115	8.97 ± 0.63	12.77 ± 2.48	11.44 ± 7.88
153	12.45 ± 0.89	19.52 ± 3.29	6.25 ± 9.43
221	18.87 ± 1.22	27.43 ± 4.48	16.28 ± 19.08
281	23.58 ± 1.50	33.17 ± 5.24	6.78 ± 19.62
353	28.23 ± 1.76	44.35 ± 6.08	25.05 ± 29.16
60^o	$\cdot 10^{-2}$	$\cdot 10^{-2}$	$\cdot 10^{-2}$
115	5.84 ± 0.52	7.68 ± 1.06	0.50 ± 0.23
153	7.90 ± 0.74	9.90 ± 1.36	0.69 ± 0.29
221	10.99 ± 1.02	15.12 ± 1.90	1.10 ± 0.37
281	12.92 ± 1.19	18.10 ± 2.19	1.38 ± 0.40
353	14.75 ± 1.36	21.36 ± 2.48	1.38 ± 0.44

Table VI
INTEGRATED DEUTERON PRODUCTION CROSS SECTIONS IN THE $[20-600$ MeV$]$ ENERGY RANGE MEASURED AT DIFFERENT BEAM ENERGIES AND AT DIFFERENT ANGLES.

E^{C}_{kin} $[MeV/u]$	σ^{d}_{C} [barn $/sr$]	σ^{d}_{O} [barn $/sr$]	σ^{d}_{H} [barn $/sr$]
90^o	$\cdot 10^{-3}$	$\cdot 10^{-3}$	$\cdot 10^{-5}$
115	1.04 ± 0.25	1.28 ± 0.58	0.15 ± 1.34
153	1.89 ± 0.45	2.41 ± 1.01	3.39 ± 6.54
221	2.77 ± 0.80	3.80 ± 1.51	4.44 ± 4.44
281	3.92 ± 1.05	5.42 ± 1.95	0.33 ± 1.31
353	4.57 ± 1.06	7.36 ± 2.24	6.98 ± 7.77
60^o	$\cdot 10^{-2}$	$\cdot 10^{-2}$	$\cdot 10^{-4}$
115	1.46 ± 0.44	1.90 ± 0.65	1.68 ± 3.32
153	2.16 ± 0.67	3.06 ± 1.01	1.72 ± 3.73
221	3.11 ± 1.04	4.42 ± 1.54	1.40 ± 4.07
281	3.66 ± 1.28	5.62 ± 2.00	1.28 ± 4.41
353	3.90 ± 1.44	6.19 ± 2.29	2.69 ± 6.32

The total measurement uncertainty for protons at 90 degrees is of about $6-7\%$ for carbon, about $14-20\%$ for oxygen and about $70-290\%$ for hydrogen elements. In the case of oxygen and, especially, in the case of hydrogen the statistical uncertainty dominates the achievable precision. The systematic uncertainty due to the limited precision achievable in determining the mixing matrix contributions dominates the d and t measurements, except for the case of the hydrogen element, where it is always the statistical uncertainty that limits the result precision.

This is the author's version of an article that has been published in this journal. Changes were made to this version by the publisher prior to publication.
The final version of record is available at http://dx.doi.org/10.1109/TRPMS.2020.2972197

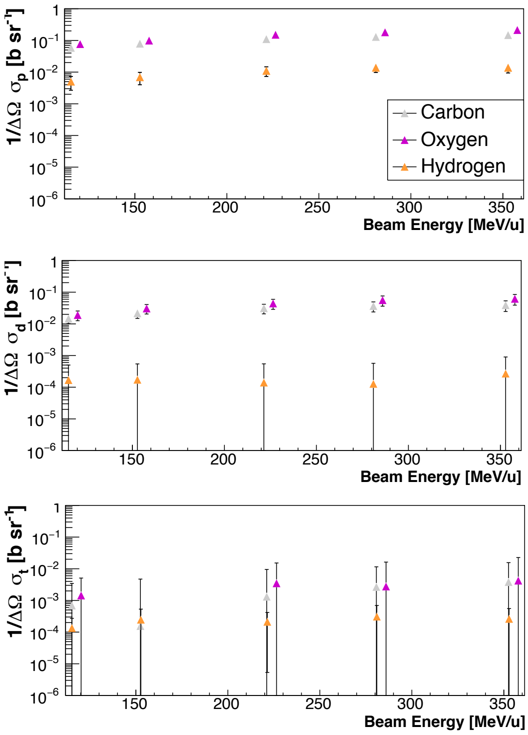

Figure 10. The cross sections integrated in the $[20-600]$ MeV fragment kinetic energy range for p (top), d (middle) and t (bottom) fragments produced in carbon (gray), oxygen (magenta) and hydrogen (orange) elements are shown as a function of the beam kinetic energy. The data refer to the 60 degrees arm. A 5 MeV shift has been applied for oxygen data in order to ease the readability of the results.

Table VII
INTEGRATED TRITON PRODUCTION CROSS SECTIONS IN THE $[20-600$ MeV$]$ ENERGY RANGE MEASURED AT DIFFERENT BEAM ENERGIES AND AT DIFFERENT ANGLES.

E^C_{kin} $[MeV/u]$	σ^t_C [barn $/sr$]	σ^t_O [barn $/sr$]	σ^t_H [barn $/sr$]
90^o	$\cdot 10^{-4}$	$\cdot 10^{-4}$	$\cdot 10^{-5}$
115	0.93 ± 1.07	-0.21 ± -1.32	1.09 ± 1.67
153	1.33 ± 1.16	4.96 ± 2.33	2.26 ± 2.29
221	2.04 ± 2.35	5.10 ± 3.83	0.40 ± 1.77
281	5.19 ± 5.16	13.30 ± 9.41	4.02 ± 3.63
353	3.20 ± 4.73	1.99 ± 7.57	21.27 ± 8.69
60^o	$\cdot 10^{-3}$	$\cdot 10^{-3}$	$\cdot 10^{-4}$
115	0.69 ± 2.76	1.43 ± 3.65	1.34 ± 1.38
153	0.14 ± 4.56	-0.01 ± -6.44	2.46 ± 2.84
221	1.29 ± 8.21	3.48 ± 11.75	2.12 ± 2.06
281	2.54 ± 8.86	2.76 ± 13.45	3.09 ± 3.85
353	3.56 ± 11.79	4.22 ± 18.41	2.62 ± 2.93

For the Arm2, the measurement on carbon ion uncertainty is about 15% ($\sim 4\%$ statistics) for the carbon target, about 100% for the hydrogen and about 25% ($\sim 12\%$ statistics) for the oxygen element. In both angular setups the cross sections for hydrogen are found to be very small and in many cases compatible with zero. This is expected, as the comparison with already existing experimental results places the production cross section in hydrogen about two orders of magnitude below the one occurring in carbon and oxygen elements. The main limitation in the measurements precision came from the limited statistics available for the subtraction method.

A direct comparison of the obtained results with other existing measurements is not possible as no other fragmentation cross-section measurement is available for the carbon ion beams energies and experimental detection angles explored in this manuscript. A qualitative comparison is possible when discussing the energy dependent spectra: the lower energy data set ($E_{beam} = 115$ MeV) results can be compared with the results obtained at $45°$ for a similar beam energy ($E_{beam} = 95$ MeV) and published by the GANIL[3] group [7]–[9]. A similar hierarchy in the cross section can be observed, as shown in Figures. 11 for p (Top), d (Middle) and t (Bottom), when comparing the integrated production cross-section at different angles.

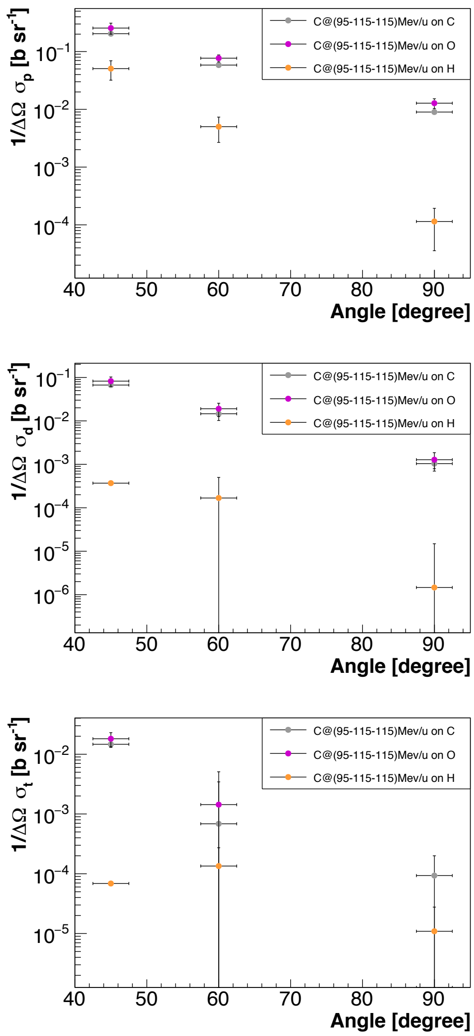

Figure 11. The integrated cross section of p (top), d (middle) and t (bottom) produced in carbon, oxygen and hydrogen as a function of the angle: 45 degrees for the GANIL experiment and 60 and 90 degrees for this study at CNAO. CNAO data refers to a carbon ion beam at 115 MeV$/u$ while the GANIL data refers to a carbon ion beam at 95 MeV$/u$.

[3] http://hadrontherapy-data.in2p3.fr/index.php/e600/e600-angular-distribution

According to [23], the integrated cross-sections at the energies explored in this paper can be evaluated by the semi-empirical equation:

$$\sigma_{tot} = \pi r_0^2 \cdot (A_P^{1/3} + A_T^{1/3} - b_0)^2 \quad (9)$$

where $r_0 = 1.31\ fm$, $b_0 = 1.0$, A_P and A_T are the projectile and target mass numbers, respectively. The σ_O/σ_C ratio is therefore expected to be about ~ 1.1. The measured ratios are listed hereafter for protons $[45^o] = 1.3 \pm 0.3$ $[60^o] = 1.3 \pm 0.2$ $[90^o] = 1.4 \pm 0.3$, deuterons $[45^o] = 1.2 \pm 0.3$ $[60^o] = 1.3 \pm 0.6$ $[90^o] = 1.2 \pm 0.6$ and tritons $[45^o] = 1.2 \pm 0.4$ $[60^o] = 2.1 \pm 10.0$ $[90^o] = -0.2 \pm 1.4$.

In all cases the results are compatible with the expected value, although in the case of tritons the large statistical uncertainty prevents to obtain a significant check at large angles (60^o and 90^o).

Conclusions

In this paper the fragmentation produced at large angles (i.e. 90 and 60 degrees) in the carbon ion interactions with C, O and H elements have been presented. The p, d and t differential production cross sections for five beam energies and two different angular setups that are relevant for particle therapy applications have been measured. The results have been qualitatively compared with the measurements performed at a different facility (GANIL) and a good agreement was obtained.

The values of $d\sigma^i_X/dE_k$ $(i = p, d, t)$ for X = C, O and H are shown in Tables VIII-XII for protons, for XIII-XVII for deuterons and for XVIII-XXII for tritons. The hydrogen contribution is, as expected, an order of magnitude lower when compared with the one of carbon and oxygen.

Both measurements at 90 and 60 degrees are of great interest when benchmarking the current state-of-art software tools adopted in the PT community. The fine tuning of the fragments production models implemented in the simulation of PT treatments is of interest not only for its application in the Treatment Planning System field, but also for the development of online monitoring tools that exploit the charged particle production in carbon ion treatments.

References

[1] M. Durante *et al.*, "Charged-particle therapy in cancer: clinical uses and future perspectives," *Nat Rev Clin Oncol.*, vol. 14(8), pp. 483–495, 2017.
[2] M. Durante and H. Paganetti, "Nuclear physics in particle therapy: a review," *Rep. Prog. Phys.*, vol. 79, no. 096702, 2016.
[3] K. Gunzert-Marx and others., "Secondary beam fragments produced by 200 mev/u 12c ions in water and their dose contributions in carbon ion radiotherapy," *New Journal of Physics*, vol. 10(7), 2008.
[4] H. Paganetti, "Range uncertainties in proton therapy and the role of monte carlo simulations," *Phys Med Biol.*, vol. 57(11), pp. R99–117., 2012.
[5] F. Tommasino, E. Scifoni, and M. Durante, "New ions for therapy," *International Journal of Particle Therapy*, vol. 2, no. 3, pp. 428–438, 2015.
[6] M. Scholz, "State-of-the-art and future prospects of ion beam therapy: physical and radiobiological aspects," *IEEE Trans Rad Plasma Med Sc*, 2019.
[7] J. Dudouet *et al.*, "Comparison of two analysis methods for nuclear reaction measurements of 12c +12c interactions at 95 mev/u for hadron therapy," *NIM*, vol. 715, pp. 98–104, 2013.
[8] J. Dudouet *et al.*, "Double-differential fragmentation cross-section measurements of 95 mev/nucleon 12c beams on thin targets for hadron therapy," *Phys. Rev. C*, vol. 88, p. 024606, 2013.
[9] J. Dudouet *et al.*, "Erratum: Double-differential fragmentation cross-section measurements of 95 mev/nucleon 12c beams on thin targets for hadron therapy," *Phys. Rev. C*, vol. 89, p. 069904, 2014.
[10] E. Haettner *et al.*, "Experimental study of nuclear fragmentation of 200 and 400 mev/u 12c ions in water for applications in particle therapy," *Phys. Med. Biol.*, vol. 58(23), 2013.
[11] G. Traini *et al.*, "Design of a new tracking device for on-line beam range monitor in carbon therapy," *Physica Medica*, vol. 34, pp. 18–27, 2017.
[12] S. Mattiazzo *et al.*, "impact: An innovative tracker and calorimeter for proton computed tomography," *IEEE Trans Rad Plasma Med Sc*, vol. 2(4), 2018.
[13] D. Mazzucconi *et al.*, "Mixed particle beam for simultaneous treatment and online range verification in carbon ion therapy: Proof-of-concept study," *Med. Phys.*, vol. 45(11), 2018.
[14] D. L. Presti *et al.*, "An innovative proton tracking system for qualification of particle beam in real-time," *IEEE Trans Rad Plasma Med Sc*, vol. 1(3), 2017.
[15] K. Parodi, "Latest developments in in-vivo imaging for proton therapy," *British Institute of Radiology*, 2019.
[16] S. Muraro *et al.*, "Monitoring of hadrontherapy treatments by means of charged particle detection," *Front. Oncol.*, 2016.
[17] L. Magallanes *et al.*, "Upgrading an integrating carbon ion transmission imaging system with active scanning beam delivery towards low dose ion imaging," *IEEE Trans Rad Plasma Med Sc*, 2019.
[18] T. Bohlen *et al.*, "The fluka code: Developments and challenges for high energy and medical applications," *Nuclear Data Sheets*, vol. 120, pp. 211–214, 2014.
[19] G. Battistoni *et al.*, "The fluka code: An accurate simulation tool for particle therapy.," *Front. Oncol*, vol. 6:116, 2016.
[20] C. P. Karger *et al.*, "Dosimetry for ion beam radiotherapy," *Phys. Med. Biol.*, vol. 55, p. R193R234, 2010.
[21] P. Andreo *et al.*, "Iaea trs-398," *IAEA*, 2006.
[22] M. Donetti, "Privat communication," 2019.
[23] S. Cecchini *et al.*, "Fragmentation cross sections of fe26+,si14+and c6+ions of 0.310agev on polyethylene,cr39 and aluminum targets," *Nuclear Physics A*, vol. 807, pp. 206–213, 2008.

Acknowledgment

Authors sincerely thank Marco Magi (*Dipartimento di Scienze di Base e Applicate per l'Ingegneria*, Sapienza Università di Roma) for his valuable effort in the construction of several mechanical supports. We are indebted to CNAO particle therapy center for encouraging this measurement, made possible by its support and by the help of the whole CNAO staff. This work has been partially supported by the Tuscany Government, POR FSE 2014 -2020, through the PETRA - INFN-RT2 172800 Project.

Appendix A
Differential Cross Section on C,O,H Elements

The differential cross sections for both protons (VIII-XII) and deuterons (XIII-XVII) are reported as a function of the fragment kinetic energy, $E^{p,d}_{bin}$ for the different target elements: C, O, H. For each energy bin the energy resolution δ_E is explicitly shown. The values are available for the five different carbon ion beam energies. In the 90 degrees setup the differential cross sections, obtained with hydrogen target, are in some cases compatible with zero. The uncertainty reported in the Tables is the squared sum of the statistical and systematic contributions.

Table VIII
PROTON PRODUCTION DIFFERENTIAL CROSS SECTION IN THE DIFFERENT ELEMENTS FROM CARBON ION BEAM ENERGY OF 115 MeV/u.

E^p_{bin} $[MeV]$	δ_E $[MeV]$	$d\sigma^p_C/dE_k$ [b/sr/MeV]	$d\sigma^p_O/dE_k$ [b/sr/MeV]	$d\sigma^p_H/dE_k$ [b/sr/MeV]
90^o		$\cdot 10^{-4}$	$\cdot 10^{-4}$	$\cdot 10^{-4}$
30-35	2	5.4 ± 0.8	17.4 ± 12.4	2.8 ± 1.8
35-40	2	3.3 ± 0.4	3.5 ± 2.4	-0.1 ± 0.5
40-60	2	1.9 ± 0.1	3.1 ± 0.7	-0.3 ± 0.1
60-80	4	0.6 ± 0.1	1.2 ± 0.4	0.1 ± 0.1
80-100	6	0.4 ± 0.1	0.3 ± 0.2	-
100-120	10	0.2 ± 0.1	0.5 ± 0.1	-
120-140	14	0.1 ± 0.1	0.2 ± 0.1	-
60^o		$\cdot 10^{-4}$	$\cdot 10^{-4}$	$\cdot 10^{-4}$
30-35	2	15.1 ± 2.1	-6.5 ± 26.6	13.8 ± 5.4
35-40	2	11.2 ± 1.2	11.1 ± 10.3	3.8 ± 1.9
40-60	2	9.3 ± 0.5	10.2 ± 3.7	1.2 ± 0.7
60-80	3	6.3 ± 0.4	7.6 ± 2.5	0.4 ± 0.5
80-100	5	3.3 ± 0.2	3.7 ± 1.4	0.3 ± 0.3
100-120	8	1.6 ± 0.1	2.1 ± 0.7	-0.0 ± 0.1
120-140	10	0.8 ± 0.1	1.2 ± 0.4	0.0 ± 0.1
140-160	13	0.4 ± 0.1	0.8 ± 0.2	-0.1 ± 0.1
160-180	16	0.3 ± 0.1	0.4 ± 0.1	-
180-200	20	0.1 ± 0.1	0.1 ± 0.1	-
200-230	23	0.1 ± 0.1	0.1 ± 0.1	-
230-260	27	-	0.1 ± 0.1	-

Table IX
PROTON PRODUCTION DIFFERENTIAL CROSS SECTION IN THE DIFFERENT ELEMENTS FROM CARBON ION BEAM ENERGY OF 153 MeV/u.

E^p_{bin} $[MeV]$	δ_E $[MeV]$	$d\sigma^p_C/dE_k$ [b/sr/MeV]	$d\sigma^p_O/dE_k$ [b/sr/MeV]	$d\sigma^p_H/dE_k$ [b/sr/MeV]
90^o		$\cdot 10^{-4}$	$\cdot 10^{-4}$	$\cdot 10^{-4}$
30-35	0	6.7 ± 1.0	18.9 ± 14.6	3.2 ± 2.2
35-40	2	4.0 ± 0.4	3.3 ± 2.9	0.0 ± 0.6
40-60	2	2.6 ± 0.1	3.4 ± 0.9	-0.3 ± 0.2
60-80	4	1.0 ± 0.1	1.4 ± 0.5	0.1 ± 0.1
80-100	6	0.5 ± 0.1	0.3 ± 0.3	-0.0 ± 0.1
100-120	10	0.2 ± 0.1	0.1 ± 0.2	-
120-140	14	0.1 ± 0.1	0.0 ± 0.1	-
60^o		$\cdot 10^{-4}$	$\cdot 10^{-4}$	$\cdot 10^{-4}$
30-35	2	20.6 ± 2.9	-4.8 ± 35.5	17.8 ± 7.2
35-40	2	14.9 ± 1.6	13.1 ± 13.2	4.5 ± 2.5
40-60	2	10.0 ± 0.6	9.4 ± 4.1	2.0 ± 0.8
60-80	3	5.4 ± 0.3	6.4 ± 2.3	1.0 ± 0.4
80-100	5	2.7 ± 0.2	2.8 ± 1.2	0.6 ± 0.2
100-120	8	1.5 ± 0.1	1.5 ± 0.6	0.1 ± 0.1
120-140	10	0.7 ± 0.1	0.7 ± 0.3	0.1 ± 0.1
140-160	13	0.5 ± 0.1	0.5 ± 0.2	-
160-180	16	0.3 ± 0.1	0.4 ± 0.2	-
180-200	20	0.1 ± 0.1	0.1 ± 0.1	-
200-230	23	0.1 ± 0.1	0.1 ± 0.1	-

Table X
PROTON PRODUCTION DIFFERENTIAL CROSS SECTION IN THE DIFFERENT ELEMENTS FROM CARBON ION BEAM ENERGY OF 221 MeV/u.

E^p_{bin} $[MeV]$	δ_E $[MeV]$	$d\sigma^p_C/dE_k$ [b/sr/MeV]	$d\sigma^p_O/dE_k$ [b/sr/MeV]	$d\sigma^p_H/dE_k$ [b/sr/MeV]
90^o		$\cdot 10^{-4}$	$\cdot 10^{-4}$	$\cdot 10^{-4}$
30-35	0	8.6 ± 1.3	23.3 ± 19.5	4.9 ± 2.9
35-40	2	5.2 ± 0.6	5.9 ± 3.8	-0.2 ± 0.7
40-60	2	3.5 ± 0.2	4.9 ± 1.2	-0.4 ± 0.2
60-80	4	1.6 ± 0.1	2.1 ± 0.7	0.1 ± 0.1
80-100	6	0.9 ± 0.1	0.5 ± 0.4	0.0 ± 0.1
100-120	10	0.4 ± 0.1	0.5 ± 0.2	0.1 ± 0.1
120-140	14	0.2 ± 0.1	0.2 ± 0.1	-
140-180	18	0.1 ± 0.1	0.1 ± 0.1	-
60^o		$\cdot 10^{-4}$	$\cdot 10^{-4}$	$\cdot 10^{-4}$
30-35	2	24.4 ± 3.4	-1.7 ± 41.5	20.0 ± 8.4
35-40	2	18.4 ± 2.0	17.4 ± 16.5	5.7 ± 3.1
40-60	2	14.4 ± 0.8	15.3 ± 5.8	2.7 ± 1.1
60-80	3	10.0 ± 0.6	11.5 ± 4.3	2.5 ± 0.8
80-100	5	6.3 ± 0.4	5.7 ± 3.1	2.6 ± 0.6
100-120	8	3.9 ± 0.2	4.8 ± 1.8	1.0 ± 0.3
120-140	10	2.2 ± 0.1	2.4 ± 1.0	0.4 ± 0.2
140-160	13	1.2 ± 0.1	1.8 ± 0.5	-0.1 ± 0.1
160-180	16	0.7 ± 0.1	1.1 ± 0.3	-0.0 ± 0.1
180-200	20	0.4 ± 0.1	0.3 ± 0.2	-
200-230	23	0.2 ± 0.1	0.2 ± 0.1	-
230-260	27	0.1 ± 0.1	0.2 ± 0.1	-
260-290	33	0.1 ± 0.1	0.2 ± 0.1	-
290-350	40	-	0.1 ± 0.1	-

Table XI
PROTON PRODUCTION DIFFERENTIAL CROSS SECTION IN THE DIFFERENT ELEMENTS FROM CARBON ION BEAM ENERGY OF 281 MeV/u.

E^p_{bin} $[MeV]$	δ_E $[MeV]$	$d\sigma^p_C/dE_k$ [b/sr/MeV]	$d\sigma^p_O/dE_k$ [b/sr/MeV]	$d\sigma^p_H/dE_k$ [b/sr/MeV]
90^o		$\cdot 10^{-4}$	$\cdot 10^{-4}$	$\cdot 10^{-4}$
30-35	0	10.0 ± 1.5	30.7 ± 22.8	5.3 ± 3.3
35-40	2	5.8 ± 0.6	4.8 ± 4.4	0.4 ± 0.9
40-60	2	4.3 ± 0.2	6.2 ± 1.5	-0.5 ± 0.3
60-80	4	2.0 ± 0.1	2.6 ± 0.8	0.1 ± 0.2
80-100	6	1.0 ± 0.1	0.8 ± 0.5	0.1 ± 0.1
100-120	10	0.6 ± 0.1	0.6 ± 0.3	0.0 ± 0.1
120-140	14	0.3 ± 0.1	0.2 ± 0.2	0.1 ± 0.1
140-180	18	0.1 ± 0.1	0.2 ± 0.1	-
180-250	25	-	0.1 ± 0.1	-
60^o		$\cdot 10^{-4}$	$\cdot 10^{-4}$	$\cdot 10^{-4}$
30-35	2	24.9 ± 3.5	0.6 ± 41.2	19.0 ± 8.3
35-40	2	18.7 ± 2.0	17.6 ± 16.5	5.4 ± 3.1
40-60	2	15.9 ± 0.9	16.4 ± 6.3	2.6 ± 1.2
60-80	3	12.1 ± 0.7	14.1 ± 5.3	3.2 ± 1.0
80-100	5	8.8 ± 0.5	8.6 ± 4.3	3.8 ± 0.8
100-120	8	6.3 ± 0.4	8.6 ± 3.0	1.7 ± 0.5
120-140	10	4.0 ± 0.2	4.3 ± 1.9	1.2 ± 0.4
140-160	13	2.4 ± 0.2	3.3 ± 1.0	0.1 ± 0.2
160-180	16	1.4 ± 0.1	2.4 ± 0.7	0.0 ± 0.1
180-200	20	0.8 ± 0.1	0.6 ± 0.4	0.0 ± 0.1
200-230	23	0.4 ± 0.1	0.5 ± 0.2	-
230-260	27	0.2 ± 0.1	0.3 ± 0.1	-
260-290	33	0.1 ± 0.1	0.1 ± 0.1	-
290-350	40	-	0.1 ± 0.1	-

This is the author's version of an article that has been published in this journal. Changes were made to this version by the publisher prior to publication.
The final version of record is available at http://dx.doi.org/10.1109/TRPMS.2020.2972197

Table XII
PROTON PRODUCTION DIFFERENTIAL CROSS SECTION IN THE DIFFERENT ELEMENTS FROM CARBON ION BEAM ENERGY OF 353 MeV/u.

E^p_{bin} $[MeV]$	δ_E $[MeV]$	$d\sigma^p_C/dE_k$ [b/sr/MeV]	$d\sigma^p_O/dE_k$ [b/sr/MeV]	$d\sigma^p_H/dE_k$ [b/sr/MeV]
90^o		$\cdot 10^{-4}$	$\cdot 10^{-4}$	$\cdot 10^{-4}$
30-35	0	11.1 ± 1.7	32.7 ± 25.3	6.0 ± 3.7
35-40	2	6.9 ± 0.7	7.0 ± 5.0	-0.1 ± 1.0
40-60	2	4.9 ± 0.3	6.8 ± 1.7	-0.4 ± 0.3
60-80	4	2.4 ± 0.1	3.1 ± 1.0	0.2 ± 0.2
80-100	6	1.4 ± 0.1	1.1 ± 0.6	0.1 ± 0.1
100-120	10	0.7 ± 0.1	0.9 ± 0.3	0.1 ± 0.1
120-140	14	0.4 ± 0.1	0.3 ± 0.2	0.1 ± 0.1
140-180	18	0.2 ± 0.1	0.4 ± 0.1	-
180-250	25	0.1 ± 0.1	0.1 ± 0.1	-
60^o		$\cdot 10^{-4}$	$\cdot 10^{-4}$	$\cdot 10^{-4}$
30-35	2	24.0 ± 3.4	-5.1 ± 39.4	18.6 ± 8.0
35-40	2	17.8 ± 2.0	18.9 ± 15.8	5.0 ± 3.0
40-60	2	15.7 ± 0.9	17.3 ± 6.3	2.6 ± 1.2
60-80	3	13.0 ± 0.7	14.8 ± 5.6	3.4 ± 1.1
80-100	5	10.4 ± 0.6	10.9 ± 5.2	4.5 ± 1.0
100-120	8	8.4 ± 0.5	10.7 ± 4.0	2.7 ± 0.7
120-140	10	6.0 ± 0.4	7.7 ± 3.0	2.0 ± 0.5
140-160	13	4.3 ± 0.3	6.1 ± 1.8	0.2 ± 0.3
160-180	16	2.6 ± 0.2	4.0 ± 1.3	0.5 ± 0.2
180-200	20	1.6 ± 0.1	1.2 ± 0.8	0.4 ± 0.1
200-230	23	0.8 ± 0.1	1.2 ± 0.3	0.1 ± 0.1
230-260	27	0.5 ± 0.1	0.7 ± 0.2	-
260-290	33	0.2 ± 0.1	0.4 ± 0.1	-
290-350	40	0.1 ± 0.1	0.2 ± 0.1	-

Table XIII
DEUTERON PRODUCTION DIFFERENTIAL CROSS SECTION IN THE DIFFERENT ELEMENTS FROM CARBON ION BEAM ENERGY OF 115 MeV/u.

E^d_{bin} $[MeV]$	δ_E $[MeV]$	$d\sigma^d_C/dE_k$ [b/sr/MeV]	$d\sigma^d_O/dE_k$ [b/sr/MeV]	$d\sigma^d_H/dE_k$ [b/sr/MeV]
90^o		$\cdot 10^{-5}$	$\cdot 10^{-5}$	$\cdot 10^{-5}$
40-60	0	4.2 ± 0.3	5.9 ± 2.6	0.1 ± 0.5
60-80	3	1.7 ± 0.2	2.6 ± 1.3	-0.1 ± 0.2
80-100	5	0.7 ± 0.1	0.7 ± 0.8	-0.0 ± 0.2
100-120	7	0.3 ± 0.1	0.3 ± 0.5	0.1 ± 0.1
120-140	10	0.1 ± 0.1	0.1 ± 0.4	0.0 ± 0.1
140-180	13	-	0.0 ± 0.1	-
180-250	18	-	0.0 ± 0.1	-
60^o		$\cdot 10^{-5}$	$\cdot 10^{-5}$	$\cdot 10^{-5}$
40-60	2	31.4 ± 2.8	35.9 ± 20.1	1.6 ± 3.8
60-80	2	17.9 ± 1.4	19.1 ± 11.2	4.4 ± 2.1
80-100	4	14.9 ± 1.2	12.9 ± 7.9	0.1 ± 1.5
100-120	6	9.8 ± 0.8	15.1 ± 5.7	0.3 ± 1.0
120-140	8	6.2 ± 0.5	13.3 ± 3.6	-0.5 ± 0.6
140-160	10	3.9 ± 0.4	2.7 ± 2.2	-0.5 ± 0.4
160-180	12	2.0 ± 0.2	2.6 ± 1.2	-0.4 ± 0.2
180-200	15	0.9 ± 0.1	0.9 ± 0.7	0.1 ± 0.1
200-230	17	0.4 ± 0.1	0.3 ± 0.4	0.0 ± 0.1
230-260	21	0.2 ± 0.1	0.3 ± 0.2	-0.1 ± 0.1
260-290	26	0.1 ± 0.1	0.0 ± 0.1	-

Table XIV
DEUTERON PRODUCTION DIFFERENTIAL CROSS SECTION IN THE DIFFERENT ELEMENTS FROM CARBON ION BEAM ENERGY OF 153 MeV/u.

E^d_{bin} $[MeV]$	δ_E $[MeV]$	$d\sigma^d_C/dE_k$ [b/sr/MeV]	$d\sigma^d_O/dE_k$ [b/sr/MeV]	$d\sigma^d_H/dE_k$ [b/sr/MeV]
90^o		$\cdot 10^{-5}$	$\cdot 10^{-5}$	$\cdot 10^{-5}$
40-60	0	14.2 ± 1.2	11.7 ± 8.5	1.1 ± 1.6
60-80	3	6.9 ± 0.6	6.7 ± 3.5	-1.4 ± 0.7
80-100	5	3.1 ± 0.4	4.0 ± 2.0	-0.6 ± 0.4
100-120	7	1.3 ± 0.2	1.9 ± 1.1	-0.2 ± 0.2
120-140	10	0.5 ± 0.1	0.3 ± 0.7	0.0 ± 0.1
140-180	13	0.2 ± 0.1	0.4 ± 0.2	-
180-250	18	-	0.0 ± 0.1	-
60^o		$\cdot 10^{-5}$	$\cdot 10^{-5}$	$\cdot 10^{-5}$
40-60	2	39.8 ± 3.5	27.6 ± 24.5	2.0 ± 4.8
60-80	2	18.3 ± 1.4	9.5 ± 11.0	4.3 ± 2.2
80-100	4	12.7 ± 1.0	6.8 ± 6.4	-0.5 ± 1.3
100-120	6	6.7 ± 0.6	5.8 ± 3.8	0.3 ± 0.7
120-140	8	4.1 ± 0.4	7.0 ± 2.5	-0.2 ± 0.4
140-160	10	2.8 ± 0.3	2.5 ± 1.6	-0.4 ± 0.3
160-180	12	1.5 ± 0.2	0.5 ± 1.0	0.1 ± 0.2
180-200	15	0.8 ± 0.1	1.6 ± 0.7	0.1 ± 0.1
200-230	17	0.5 ± 0.1	0.3 ± 0.4	-0.0 ± 0.1
230-260	21	0.2 ± 0.1	0.2 ± 0.3	-0.0 ± 0.1
260-290	26	0.1 ± 0.1	0.3 ± 0.2	-0.1 ± 0.1
290-350	31	-	0.1 ± 0.1	-

Table XV
DEUTERON PRODUCTION DIFFERENTIAL CROSS SECTION IN THE DIFFERENT ELEMENTS FROM CARBON ION BEAM ENERGY OF 221 MeV/u.

E^d_{bin} $[MeV]$	δ_E $[MeV]$	$d\sigma^d_C/dE_k$ [b/sr/MeV]	$d\sigma^d_O/dE_k$ [b/sr/MeV]	$d\sigma^d_H/dE_k$ [b/sr/MeV]
90^o		$\cdot 10^{-5}$	$\cdot 10^{-5}$	$\cdot 10^{-5}$
40-60	0	16.8 ± 1.4	19.8 ± 10.3	1.1 ± 1.9
60-80	3	8.3 ± 0.7	8.4 ± 4.4	-0.6 ± 0.8
80-100	5	4.8 ± 0.5	7.9 ± 2.8	-0.9 ± 0.5
100-120	7	2.3 ± 0.3	3.0 ± 1.6	-0.1 ± 0.3
120-140	10	1.1 ± 0.2	2.1 ± 1.1	0.1 ± 0.2
140-180	13	0.4 ± 0.1	0.5 ± 0.4	0.1 ± 0.1
180-250	18	0.1 ± 0.1	0.3 ± 0.2	-
250-350	28	-	0.0 ± 0.1	-
60^o		$\cdot 10^{-5}$	$\cdot 10^{-5}$	$\cdot 10^{-5}$
40-60	2	36.9 ± 3.3	29.9 ± 23.9	4.1 ± 4.6
60-80	2	19.5 ± 1.5	11.0 ± 11.7	4.4 ± 2.3
80-100	4	13.6 ± 1.1	5.6 ± 7.3	0.9 ± 1.5
100-120	6	8.9 ± 0.7	9.7 ± 5.0	0.1 ± 1.0
120-140	8	5.8 ± 0.5	12.3 ± 3.4	-0.5 ± 0.6
140-160	10	4.9 ± 0.5	2.3 ± 2.6	-0.8 ± 0.5
160-180	12	3.1 ± 0.3	1.7 ± 1.8	-0.4 ± 0.4
180-200	15	2.1 ± 0.2	3.4 ± 1.3	-0.5 ± 0.3
200-230	17	1.2 ± 0.1	1.8 ± 0.7	-0.1 ± 0.1
230-260	21	0.7 ± 0.1	1.3 ± 0.5	-0.1 ± 0.1
260-290	26	0.4 ± 0.1	0.8 ± 0.4	-0.1 ± 0.1
290-350	31	0.1 ± 0.1	0.2 ± 0.1	-
350-450	38	-	0.1 ± 0.1	-

Table XVI
DEUTERON PRODUCTION DIFFERENTIAL CROSS SECTION IN THE DIFFERENT ELEMENTS FROM CARBON ION BEAM ENERGY OF 281 MeV/u.

E^d_{bin} $[MeV]$	δ_E $[MeV]$	$d\sigma^d_C/dE_k$ [b/sr/MeV]	$d\sigma^d_O/dE_k$ [b/sr/MeV]	$d\sigma^d_H/dE_k$ [b/sr/MeV]
90^o		$\cdot 10^{-5}$	$\cdot 10^{-5}$	$\cdot 10^{-5}$
40-60	0	16.2 ± 1.3	18.1 ± 10.1	1.7 ± 1.9
60-80	3	7.9 ± 0.7	8.4 ± 4.3	-0.3 ± 0.8
80-100	5	5.3 ± 0.5	7.2 ± 2.9	-1.1 ± 0.6
100-120	7	2.2 ± 0.3	2.4 ± 1.7	0.1 ± 0.3
120-140	10	1.3 ± 0.2	1.0 ± 1.1	0.1 ± 0.2
140-180	13	0.6 ± 0.1	1.1 ± 0.4	-0.1 ± 0.1
180-250	18	0.2 ± 0.1	0.4 ± 0.2	-
250-350	28	-	0.0 ± 0.1	-
60^o		$\cdot 10^{-5}$	$\cdot 10^{-5}$	$\cdot 10^{-5}$
60-80	2	17.5 ± 1.3	13.8 ± 10.5	3.6 ± 2.0
80-100	4	12.7 ± 1.0	4.5 ± 6.7	0.7 ± 1.4
100-120	6	7.9 ± 0.7	9.1 ± 4.5	0.2 ± 0.9
120-140	8	4.9 ± 0.4	9.9 ± 3.0	-0.1 ± 0.5
140-160	10	4.1 ± 0.4	2.1 ± 2.3	-0.3 ± 0.5
160-180	12	2.3 ± 0.2	1.4 ± 1.5	0.1 ± 0.3
180-200	15	1.7 ± 0.2	3.8 ± 1.3	-0.1 ± 0.2
200-230	17	1.3 ± 0.1	1.8 ± 0.8	-0.2 ± 0.1
230-260	21	0.5 ± 0.1	0.8 ± 0.4	0.1 ± 0.1
260-290	26	0.4 ± 0.1	0.6 ± 0.4	-0.0 ± 0.1
290-350	31	0.2 ± 0.1	0.3 ± 0.2	-
350-450	38	0.1 ± 0.1	0.1 ± 0.1	-

Table XVII
DEUTERON PRODUCTION DIFFERENTIAL CROSS SECTION IN THE DIFFERENT ELEMENTS FROM CARBON ION BEAM ENERGY OF 353 MeV/u.

E^d_{bin} $[MeV]$	δ_E $[MeV]$	$d\sigma^d_C/dE_k$ [b/sr/MeV]	$d\sigma^d_O/dE_k$ [b/sr/MeV]	$d\sigma^d_H/dE_k$ [b/sr/MeV]
90^o		$\cdot 10^{-5}$	$\cdot 10^{-5}$	$\cdot 10^{-5}$
40-60	0	17.1 ± 1.4	23.0 ± 10.0	-0.2 ± 1.9
60-80	3	8.2 ± 0.7	9.6 ± 4.3	-0.9 ± 0.8
80-100	5	3.9 ± 0.4	6.1 ± 2.6	-0.3 ± 0.5
100-120	7	2.0 ± 0.2	2.6 ± 1.5	0.1 ± 0.3
120-140	10	1.3 ± 0.2	1.7 ± 1.1	0.1 ± 0.2
140-180	13	0.6 ± 0.1	0.9 ± 0.4	-0.1 ± 0.1
180-250	18	0.1 ± 0.1	0.3 ± 0.2	-
250-350	28	-	0.0 ± 0.1	-
60^o		$\cdot 10^{-5}$	$\cdot 10^{-5}$	$\cdot 10^{-5}$
40-60	2	30.4 ± 2.7	24.4 ± 19.8	3.6 ± 3.8
60-80	2	15.3 ± 1.2	12.2 ± 9.2	3.1 ± 1.8
80-100	4	10.1 ± 0.8	5.9 ± 5.5	0.7 ± 1.1
100-120	6	6.4 ± 0.5	6.7 ± 3.7	0.2 ± 0.7
120-140	8	4.3 ± 0.4	9.2 ± 2.6	-0.3 ± 0.5
140-160	10	3.4 ± 0.3	2.9 ± 1.9	-0.4 ± 0.4
160-180	12	1.9 ± 0.2	1.7 ± 1.3	-0.0 ± 0.3
180-200	15	1.5 ± 0.2	2.9 ± 1.1	-0.2 ± 0.2
200-230	17	0.9 ± 0.1	1.2 ± 0.6	-0.0 ± 0.1
230-260	21	0.6 ± 0.1	1.3 ± 0.4	-0.2 ± 0.1
260-290	26	0.3 ± 0.1	0.6 ± 0.3	-0.0 ± 0.1
290-350	31	0.2 ± 0.1	0.1 ± 0.2	-
350-450	38	-	0.0 ± 0.1	-

Table XVIII
TRITONS PRODUCTION DIFFERENTIAL CROSS SECTION IN THE DIFFERENT ELEMENTS FROM CARBON ION BEAM ENERGY OF 115 MeV/u.

E^t_{bin} $[MeV]$	δ_E $[MeV]$	$d\sigma^t_C/dE_k$ [b/sr/MeV]	$d\sigma^t_O/dE_k$ [b/sr/MeV]	$d\sigma^t_H/dE_k$ [b/sr/MeV]
90^o		$\cdot 10^{-6}$	$\cdot 10^{-6}$	$\cdot 10^{-6}$
40-60	0	6.9 ± 0.9	2.0 ± 8.4	1.8 ± 1.6
60-80	2	1.8 ± 0.6	-1.1 ± 3.2	0.2 ± 0.7
80-100	4	1.2 ± 0.5	1.0 ± 2.7	-0.3 ± 0.5
100-120	6	0.9 ± 0.3	0.2 ± 1.9	-0.5 ± 0.4
120-140	8	0.1 ± 0.3	0.9 ± 1.6	-0.0 ± 0.3
140-180	11	0.1 ± 0.1	-0.0 ± 0.4	-0.0 ± 0.1
180-250	15	-	0.1 ± 0.2	-
60^o		$\cdot 10^{-6}$	$\cdot 10^{-6}$	$\cdot 10^{-6}$
40-60	2	44.4 ± 6.4	22.9 ± 52.3	13.1 ± 10.2
60-80	2	37.9 ± 4.1	12.0 ± 26.6	1.2 ± 5.4
80-100	3	25.7 ± 3.0	1.0 ± 20.2	3.2 ± 4.2
100-120	4	13.4 ± 1.7	10.2 ± 11.2	1.0 ± 2.2
120-140	7	9.8 ± 1.4	18.0 ± 8.2	-2.4 ± 1.5
140-160	8	6.4 ± 1.0	2.1 ± 6.6	0.7 ± 1.3
160-180	10	4.9 ± 0.9	8.2 ± 5.0	-1.6 ± 0.9
180-200	12	1.7 ± 0.5	3.5 ± 2.9	0.0 ± 0.5
200-230	14	1.4 ± 0.4	0.2 ± 2.1	-0.0 ± 0.4
230-260	18	0.1 ± 0.1	-0.3 ± 1.0	0.5 ± 0.2
260-290	22	0.2 ± 0.1	-0.0 ± 0.9	0.1 ± 0.2
290-350	26	-	0.1 ± 0.2	0.1 ± 0.1

Table XIX
TRITONS PRODUCTION DIFFERENTIAL CROSS SECTION IN THE DIFFERENT ELEMENTS FROM CARBON ION BEAM ENERGY OF 153 MeV/u.

E^t_{bin} $[MeV]$	δ_E $[MeV]$	$d\sigma^t_C/dE_k$ [b/sr/MeV]	$d\sigma^t_O/dE_k$ [b/sr/MeV]	$d\sigma^t_H/dE_k$ [b/sr/MeV]
90^o		$\cdot 10^{-6}$	$\cdot 10^{-6}$	$\cdot 10^{-6}$
40-60	0	31.3 ± 4.2	22.9 ± 39.7	8.7 ± 7.5
60-80	2	13.4 ± 1.8	16.9 ± 9.7	-3.4 ± 1.9
80-100	4	6.2 ± 1.4	4.5 ± 7.6	-1.1 ± 1.5
100-120	6	2.0 ± 0.8	3.0 ± 4.4	-0.7 ± 0.9
120-140	8	0.1 ± 0.5	0.4 ± 2.7	0.7 ± 0.5
140-180	11	0.1 ± 0.1	-0.0 ± 0.6	0.0 ± 0.1
180-250	15	-	0.1 ± 0.3	0.0 ± 0.1
60^o		$\cdot 10^{-6}$	$\cdot 10^{-6}$	$\cdot 10^{-6}$
40-60	2	95.1 ± 13.0	50.1 ± 101.7	18.9 ± 20.0
60-80	2	58.8 ± 6.2	38.1 ± 42.9	6.7 ± 8.4
80-100	3	32.6 ± 3.7	8.6 ± 27.3	8.3 ± 5.5
100-120	4	19.0 ± 2.3	12.8 ± 14.4	0.0 ± 2.8
120-140	7	11.3 ± 1.6	21.3 ± 8.7	-4.0 ± 1.6
140-160	8	5.2 ± 0.9	0.5 ± 5.7	0.7 ± 1.2
160-180	10	3.5 ± 0.7	4.5 ± 4.5	0.2 ± 0.9
180-200	12	1.9 ± 0.5	1.4 ± 2.9	-0.1 ± 0.6
200-230	14	0.7 ± 0.3	-0.5 ± 1.6	0.4 ± 0.3
230-260	18	0.4 ± 0.2	0.9 ± 1.0	-0.2 ± 0.2
260-290	22	0.1 ± 0.1	-0.2 ± 0.6	0.1 ± 0.1
290-350	26	0.1 ± 0.1	0.3 ± 0.4	-0.1 ± 0.1
350-450	32	-	0.1 ± 0.1	-

This is the author's version of an article that has been published in this journal. Changes were made to this version by the publisher prior to publication.
The final version of record is available at http://dx.doi.org/10.1109/TRPMS.2020.2972197

Table XX
TRITONS PRODUCTION DIFFERENTIAL CROSS SECTION IN THE DIFFERENT ELEMENTS FROM CARBON ION BEAM ENERGY OF 221 MeV/u.

E^t_{bin} $[MeV]$	δ_E $[MeV]$	$d\sigma^t_C/dE_k$ [b/sr/MeV]	$d\sigma^t_O/dE_k$ [b/sr/MeV]	$d\sigma^t_H/dE_k$ [b/sr/MeV]
90^o		$\cdot 10^{-6}$	$\cdot 10^{-6}$	$\cdot 10^{-6}$
40-60	0	35.8 ± 4.7	17.5 ± 50.6	16.9 ± 9.6
60-80	2	17.7 ± 2.1	19.1 ± 12.3	-2.2 ± 2.4
80-100	4	8.4 ± 1.7	18.5 ± 9.7	-0.9 ± 1.8
100-120	6	4.4 ± 1.0	5.1 ± 6.0	-0.1 ± 1.1
120-140	8	2.0 ± 0.7	7.0 ± 4.4	-0.6 ± 0.8
140-180	11	0.9 ± 0.3	0.9 ± 1.4	-0.3 ± 0.3
180-250	15	0.0 ± 0.1	0.0 ± 0.7	0.1 ± 0.2
250-350	25	-	0.0 ± 0.2	-
60^o		$\cdot 10^{-6}$	$\cdot 10^{-6}$	$\cdot 10^{-6}$
40-60	2	86.7 ± 11.9	14.9 ± 100.0	30.7 ± 19.9
60-80	2	64.5 ± 6.7	62.9 ± 46.7	4.7 ± 9.0
80-100	3	40.9 ± 4.5	13.0 ± 31.7	6.1 ± 6.5
100-120	4	25.4 ± 2.9	29.5 ± 18.0	-2.6 ± 3.5
120-140	7	17.0 ± 2.2	36.3 ± 12.6	-4.9 ± 2.3
140-160	8	7.4 ± 1.1	4.9 ± 8.6	3.3 ± 1.7
160-180	10	5.2 ± 0.9	15.7 ± 6.1	-0.6 ± 1.1
180-200	12	3.8 ± 0.8	4.3 ± 4.6	0.0 ± 0.9
200-230	14	2.3 ± 0.5	0.3 ± 3.0	0.5 ± 0.6
230-260	18	0.7 ± 0.3	4.1 ± 2.1	0.6 ± 0.3
260-290	22	0.5 ± 0.2	-0.0 ± 1.3	0.1 ± 0.3
290-350	26	0.2 ± 0.1	-0.0 ± 0.6	0.1 ± 0.1
350-450	32	0.1 ± 0.1	0.1 ± 0.2	-

Table XXI
TRITONS PRODUCTION DIFFERENTIAL CROSS SECTION IN THE DIFFERENT ELEMENTS FROM CARBON ION BEAM ENERGY OF 281 MeV/u.

E^t_{bin} $[MeV]$	δ_E $[MeV]$	$d\sigma^t_C/dE_k$ [b/sr/MeV]	$d\sigma^t_O/dE_k$ [b/sr/MeV]	$d\sigma^t_H/dE_k$ [b/sr/MeV]
90^o		$\cdot 10^{-6}$	$\cdot 10^{-6}$	$\cdot 10^{-6}$
40-60	0	32.2 ± 4.3	48.3 ± 54.3	20.8 ± 9.6
60-80	2	17.2 ± 2.0	18.0 ± 12.1	-1.6 ± 2.4
80-100	4	8.4 ± 1.6	18.9 ± 9.6	-1.1 ± 1.8
100-120	6	4.1 ± 1.0	10.9 ± 6.0	-0.4 ± 1.1
120-140	8	1.9 ± 0.7	5.1 ± 4.5	0.4 ± 0.8
140-180	11	1.0 ± 0.2	3.1 ± 1.5	-0.3 ± 0.3
180-250	15	0.3 ± 0.1	0.7 ± 0.8	-0.1 ± 0.2
250-350	25	0.1 ± 0.1	-0.0 ± 0.4	-0.0 ± 0.1
350-550	39	-	0.0 ± 0.1	-
60^o		$\cdot 10^{-6}$	$\cdot 10^{-6}$	$\cdot 10^{-6}$
40-60	2	80.8 ± 11.1	79.3 ± 90.2	16.6 ± 17.1
60-80	2	57.1 ± 6.0	59.2 ± 41.0	2.3 ± 7.9
80-100	3	34.0 ± 3.8	10.2 ± 27.6	7.1 ± 5.6
100-120	4	17.3 ± 2.1	17.7 ± 14.3	1.8 ± 2.8
120-140	7	13.4 ± 1.8	26.9 ± 10.3	-3.7 ± 1.9
140-160	8	7.8 ± 1.2	-5.9 ± 8.3	3.2 ± 1.7
160-180	10	6.5 ± 1.1	11.0 ± 6.7	-0.4 ± 1.2
180-200	12	3.5 ± 0.7	9.9 ± 4.4	-0.7 ± 0.8
200-230	14	2.0 ± 0.5	7.4 ± 2.9	-0.0 ± 0.5
230-260	18	1.2 ± 0.4	2.3 ± 2.3	0.3 ± 0.4
260-290	22	0.7 ± 0.2	1.3 ± 1.5	0.0 ± 0.3
290-350	26	0.4 ± 0.2	0.9 ± 0.8	-0.1 ± 0.2
350-450	32	-	0.1 ± 0.2	-

Table XXII
DEUTERON PRODUCTION DIFFERENTIAL CROSS SECTION IN THE DIFFERENT ELEMENTS FROM CARBON ION BEAM ENERGY OF 353 MeV/u.

E^t_{bin} $[MeV]$	δ_E $[MeV]$	$d\sigma^t_C/dE_k$ [b/sr/MeV]	$d\sigma^t_O/dE_k$ [b/sr/MeV]	$d\sigma^t_H/dE_k$ [b/sr/MeV]
90^o		$\cdot 10^{-6}$	$\cdot 10^{-6}$	$\cdot 10^{-6}$
40-60	0	37.2 ± 4.9	55.5 ± 51.7	11.9 ± 9.2
60-80	2	17.4 ± 2.1	30.1 ± 12.3	-3.4 ± 2.3
80-100	4	7.4 ± 1.6	17.2 ± 9.3	-0.9 ± 1.7
100-120	6	3.3 ± 0.9	6.8 ± 5.5	0.1 ± 1.0
120-140	8	2.3 ± 0.6	10.5 ± 4.2	-0.6 ± 0.7
140-180	11	0.8 ± 0.3	2.8 ± 1.5	-0.1 ± 0.3
180-250	15	0.1 ± 0.1	0.5 ± 0.7	-0.0 ± 0.1
250-350	25	-	-0.1 ± 0.3	0.0 ± 0.1
350-550	39	-	0.0 ± 0.1	-
60^o		$\cdot 10^{-6}$	$\cdot 10^{-6}$	$\cdot 10^{-6}$
40-60	2	74.3 ± 10.3	81.9 ± 81.2	11.2 ± 15.3
60-80	2	46.6 ± 5.0	59.2 ± 34.8	2.6 ± 6.6
80-100	3	28.1 ± 3.3	22.2 ± 23.5	4.7 ± 4.6
100-120	4	16.7 ± 2.1	17.8 ± 13.5	0.7 ± 2.6
120-140	7	9.6 ± 1.4	29.2 ± 8.9	-1.6 ± 1.5
140-160	8	6.3 ± 1.0	3.1 ± 7.0	1.7 ± 1.4
160-180	10	3.4 ± 0.7	11.0 ± 4.9	0.5 ± 0.8
180-200	12	3.1 ± 0.7	6.2 ± 4.0	-0.4 ± 0.7
200-230	14	2.6 ± 0.5	1.1 ± 2.9	-0.4 ± 0.6
230-260	18	0.6 ± 0.2	2.8 ± 1.8	0.4 ± 0.3
260-290	22	0.2 ± 0.1	-0.1 ± 1.3	0.7 ± 0.3
290-350	26	0.3 ± 0.1	0.2 ± 0.8	0.2 ± 0.1
350-450	32	0.1 ± 0.1	0.2 ± 0.2	-
450-650	43	-	-0.1 ± 0.1	-